Studying the effect of grain boundaries in dislocation density based crystal-plasticity finite element simulations

A. Ma, F. Roters *, D. Raabe

Max-Planck-Institut für Eisenforschung, Max-Planck-Str. 1, 40237 Düsseldorf, Germany

Abstract

A dislocation density based constitutive model for the face centered cubic crystal structure has been implemented into a crystal-plasticity finite element framework and extended to consider the mechanical interaction between mobile dislocations and grain boundaries by the authors [Ma, A., Roters, F., Raabe, D., 2006a. A dislocation density based constitutive model for crystal-plasticity FEM including geometrically necessary dislocations. Acta Materialia 54, 2169–2179; Ma, A., Roters, F., Raabe, D., 2006b. On the consideration of interactions between dislocations and grain boundaries in crystal-plasticity finite element modeling – theory, experiments, and simulations. Acta Materialia 54, 2181–2194]. The approach to model the grain boundary resistance against slip is based on the introduction of an additional activation energy into the rate equation for mobile dislocations in the vicinity of internal interfaces. This energy barrier is derived from the assumption of thermally activated dislocation penetration events through grain boundaries. The model takes full account of the geometry of the grain boundaries and of the Schmid factors of the critically stressed incoming and outgoing slip systems. In this study we focus on the influence of the one remaining model parameter which can be used to scale the obstacle strength of the grain boundary.
© 2006 Elsevier Ltd. All rights reserved.

Keywords: Statistically stored dislocation density; Geometrically necessary dislocation density; Internal variables; Constitutive equation; Fcc; Slip system; Crystal-plasticity FEM; Size effect

1. Introduction

For crystalline materials, Taylor (1938) was the first to formulate a model for the relationship between crystallographic slip, texture, texture evolution, and mechanical behavior of polycrystals. In his approach the *local* deformation for each grain is assumed to match the *global* deformation. The micro-mechanical interaction among grains is neglected in this original formulation. It is, therefore, typically referred to as *Full Constraints* model and thus locally satisfies strain equilibrium but not stress equilibrium. Based on this stiff model various

variants of *Relaxed Constraints* Taylor-based models were introduced which allow for the drop of some of the strain constraints among the grains. For single phase face centered cubic (fcc) and body centered cubic (bcc) polycrystals these various variants of Taylor-type models can to a certain extent be used for the prediction of the mechanical behavior and texture evolution (Ma et al., 2004; Van Houtte et al., 2005). In contrast to the Taylor type models the Crystal-Plasticity Finite Element Method (CPFEM) allows to satisfy both strain and stress equilibrium. The hardening behavior can be described using empirical power law formulations (Bronkhorst et al., 1992; Kalidindi et al., 1992).

However, when the simulation scale becomes smaller, conventional constitutive models may reveal some disadvantages, when they do not include any mechanical size effects. There are several explanations on the origin of this effect in the literature based on dislocation mechanisms. One explanation is that pile-ups of mobile dislocations in front of the grain boundary entail stress concentrations and, therefore, increase the resistance against further dislocation slip. A second approach assumes that strain gradients which typically build up near interfaces create extra geometrically necessary dislocations (Ashby, 1970) and, thereby, increase the slip resistance (Evers et al., 2002). In either case, interactions between mobile dislocations and grain boundaries should be carefully studied.

For the reason that crystallographic slip, i.e. movement of dislocations on distinct slip planes, is the main source of plastic deformation of most metals, it was an obvious idea to use a constitutive model based on dislocation densities as internal state variables within an crystal plasticity framework (Ma et al., 2006a,b). The model also includes the interaction of the mobile dislocations with grain boundaries, i.e. it is a joint formulation which includes the tensorial nature of elastic–plastic deformation in terms of dislocation slip, the evolution of the crystallographic texture at each material point, *nonlocal* orientation- and strain-gradient terms occurring between neighboring material points, and the *local* mechanical effects associated with interfaces. The aim is to provide a general approach for studying polycrystal micro-mechanics at small spatial scales in a crystal-plasticity finite element framework. The central problem addressed here is the local effect of grain boundaries on the hardening behavior. For this purpose we use different values for the single remaining model parameter which scales the grain boundary strength and study the influence on the *local* orientation and strain distribution.

2. The constitutive formulations

In this chapter, we briefly summarize the main aspects of the constitutive model introduced in Ma et al. (2006a,b). However, as the focus in this study is laid on the grain boundary this part of the model is described more detailed.

2.1. Kinematics

We are using the multiplicative decomposition of the the deformation gradient tensor $\mathbf{F}$ for large strains (Lee, 1969)

$$\mathbf{F} = \mathbf{F}_e \mathbf{F}_p \tag{1}$$

where $\mathbf{F}_e = \mathbf{R}_e \mathbf{U}_e$ is the elastic part comprising the stretch $\mathbf{U}_e$ and rotation $\mathbf{R}_e$ of the lattice, and $\mathbf{F}_p$ corresponds to the plastic deformation caused by dislocation slip. The rate equation for plastic deformation can then be written

$$\dot{\mathbf{F}}_p = \mathbf{L}_p \mathbf{F}_p \tag{2}$$

where $\mathbf{L}_p = \dot{\mathbf{F}}_p \mathbf{F}_p^{-1}$ is the plastic velocity gradient.

2.2. The flow rule

2.2.1. The constitutive model
The mobile dislocations slip on those crystallographic planes with the lowest Peierls potential. In fcc crystals these are the closest packed planes, namely the {1 1 1} lattice planes. The slip directions are the closest

packed directions, i.e. the $\langle 1\,1\,0 \rangle$ lattice directions, α is used as slip system index. At room temperature there are 12 active octahedral slip systems for the fcc crystal structure.

The connection between the continuum kinematic variables and the process of dislocation slip on these crystallographic slip systems is given by

$$\mathbf{L}_{\mathrm{p}} = \sum_{\alpha=1}^{N} \dot{\gamma}^{\alpha} \widetilde{\mathbf{M}}^{\alpha} \tag{3}$$

where $\dot{\gamma}^{\alpha}$ the slip rate on slip system α. The Schmid tensor $\widetilde{\mathbf{M}}^{\alpha} = \tilde{\mathbf{d}}^{\alpha} \otimes \tilde{\mathbf{n}}^{\alpha}$ describes the geometry of the slip systems mathematically, where $\tilde{\mathbf{d}}^{\alpha} = \mathbf{b}/b$ expresses the normalized slip direction, which is parallel to the Burgers vector $\mathbf{b}$ but normalized, and $\tilde{\mathbf{n}}^{\alpha}$ the slip plane normal with respect to the undistorted configuration. The sum is taken over all active slip systems, i.e. in the fcc case $N = 12$.

2.2.2. The Orowan equation as kinetic equation of state

In our approach we use the Orowan equation to calculate the plastic shear rate $\dot{\gamma}^{\alpha}$ of each slip system as function of the mobile dislocation density $\rho_{\mathrm{M}}^{\alpha}$ on that slip system

$$\dot{\gamma}^{\alpha} = \rho_{\mathrm{M}}^{\alpha} b v^{\alpha} \tag{4}$$

where the average velocity of the mobile dislocations, v^{α}, is a function of the resolved shear stress, τ^{α}, of the dislocation densities, $\rho_{\mathrm{M}}^{\alpha}$, $\rho_{\mathrm{F}}^{\alpha}$ and $\rho_{\mathrm{P}}^{\alpha}$, and of the temperature, θ, i.e.

$$v^{\alpha} = v^{\alpha}\left(\tau^{\alpha}, \rho_{\mathrm{M}}^{\alpha}, \rho_{\mathrm{F}}^{\alpha}, \rho_{\mathrm{P}}^{\alpha}, \theta\right) \tag{5}$$

The resolved shear stress τ^{α} is the projection of the stress measure onto the slip system α. As shown in Fig. 1, the mobile dislocations have to overcome resistances from forest and parallel dislocations, therefore we define the parallel dislocation density, $\rho_{\mathrm{P}}^{\alpha}$, and the forest dislocation density, $\rho_{\mathrm{F}}^{\alpha}$, for slip system α as: $\rho_{\mathrm{P}}^{\alpha}$ all of the dislocations parallel to the slip plane, and $\rho_{\mathrm{F}}^{\alpha}$ the dislocations perpendicular to the slip plane. Both, $\rho_{\mathrm{SSD}}^{\alpha}$ and $\rho_{\mathrm{GND}}^{\alpha}$ are contributing to $\rho_{\mathrm{F}}^{\alpha}$ and $\rho_{\mathrm{P}}^{\alpha}$. As outlined in Ma et al. (2006a) and Ma and Roters (2004) the following linear projections are adopted, where ρ_{GND} is split up into three scalar contributions $(\rho_{\mathrm{GNDs}}, \rho_{\mathrm{GNDet}}, \rho_{\mathrm{PGNDen}})$ as introduced in Section 3

$$\rho_{\mathrm{F}}^{\alpha} = \sum_{\beta=1}^{N} \chi^{\alpha,\beta} \big[\rho_{\mathrm{SSD}}^{\beta} \big| \cos(\tilde{\mathbf{n}}^{\alpha}, \tilde{\mathbf{t}}^{\beta}) \big| + \big| \rho_{\mathrm{GNDs}}^{\beta} \cos(\tilde{\mathbf{n}}^{\alpha}, \tilde{\mathbf{d}}^{\beta}) \big|$$

$$+ \big| \rho_{\mathrm{GNDet}}^{\beta} \cos(\tilde{\mathbf{n}}^{\alpha}, \tilde{\mathbf{t}}^{\beta}) \big| + \big| \rho_{\mathrm{GNDen}}^{\beta} \cos(\tilde{\mathbf{n}}^{\alpha}, \tilde{\mathbf{n}}^{\beta}) \big| \big] \tag{6}$$

$$\rho_{\mathrm{P}}^{\alpha} = \sum_{\beta=1}^{N} \chi^{\alpha\beta} \big[\rho_{\mathrm{SSD}}^{\beta} \big| \sin(\tilde{\mathbf{n}}^{\alpha}, \tilde{\mathbf{t}}^{\beta}) \big| + \big| \rho_{\mathrm{GNDs}}^{\beta} \sin(\tilde{\mathbf{n}}^{\alpha}, \tilde{\mathbf{d}}^{\beta}) \big|$$

$$+ \big| \rho_{\mathrm{GNDet}}^{\beta} \sin(\tilde{\mathbf{n}}^{\alpha}, \tilde{\mathbf{t}}^{\beta}) \big| + \big| \rho_{\mathrm{GNDen}}^{\beta} \sin(\tilde{\mathbf{n}}^{\alpha}, \tilde{\mathbf{n}}^{\beta}) \big| \big] \tag{7}$$
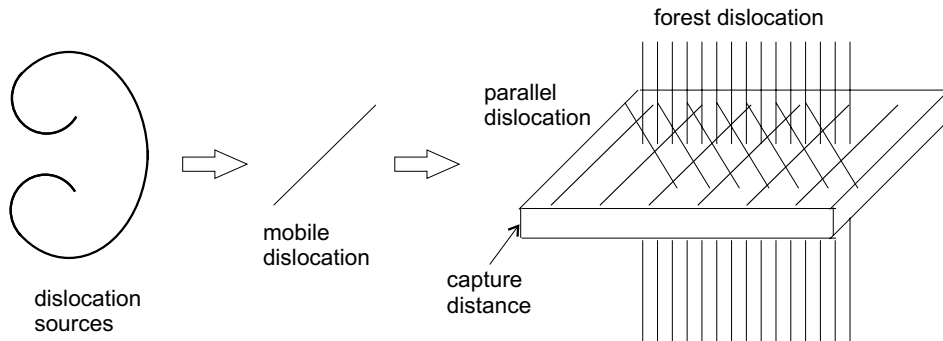
Fig. 1. Schematic drawing of the slip mechanism for the fcc crystal structure: a mobile dislocation is generated by a frank-read source, in order to move it must overcome the resistances of forest and parallel dislocations with the help of the external stress.

Here the absolute value of the GND density is used, i.e. the sign of its net Burgers vector is ignored. As a direct result no kinematic hardening can be predicted in this framework, which is, however, less relevant in case of unidirectional loading. Here we introduce the interaction strength, $\chi^{\alpha\beta}$, between different slip systems, which includes the self-interaction strength, coplanar interaction strength, cross slip strength, glissile junction strength, Hirth lock strength, and Lomer–Cottrell lock strength (Ma et al., 2006a; Ma and Roters, 2004; Arsenlis and Parks, 2002).

2.2.3. Relation between mobile and immobile dislocation densities

When integrating the velocity equation (5) into the Orowan equation (4), it becomes apparent that the shear rate $\dot{\gamma}^\alpha$ is a nonlinear function of ρ_M^α. From Ma et al. (2006a), Ma and Roters (2004) and Roters (2003) we know, that by applying the principle of maximum plastic dissipation for the external resolved shear stress during the plastic deformation[1]

$$\left(\frac{\partial \dot{\gamma}^\alpha}{\partial \rho_M^\alpha}\right)_{\tau^\alpha, \rho_F^\alpha, \rho_P^\alpha, \theta} = 0 \tag{8}$$

a scaling relation can be derived for the homogeneous dislocation structure which amounts to

$$\rho_M^\alpha \approx B\theta\sqrt{\rho_P^\alpha \rho_F^\alpha} \tag{9}$$

with

$$B = \frac{2k_B}{c_1 c_2 c_3 G b^3}. \tag{10}$$

where c_1, c_2, c_3 are constants, G is the shear modulus, b is the magnitude of the Burgers vector, θ is the absolute temperature, and k_B is the Boltzmann constant.

This means that the mobile dislocation density is proportional to the geometric mean of the parallel and the forest dislocation densities, and follows a linear relationship with the temperature. Eq. (9) forms a constraint equation for the dislocation structure, by which the dislocation structure with three sets of independent internal variables (ρ_M^α, ρ_{SSD}^α, ρ_{GND}^α, $\alpha = 1, N$) has been reduced to one with only two sets of independent internal variables (ρ_{SSD}^α, ρ_{GND}^α, $\alpha = 1, N$).

2.2.4. The flow rule based on dislocation mechanisms

Most flow rules in the literature contain a constant reference shear rate and a constant rate sensitivity exponent. In Ma et al. (2006a), a new flow rule was derived based on the dislocation slip mechanism, which also includes a reference shear rate which is, however, formulated as a function of the dislocation density and the temperature.[2] The new flow rule reads

$$\dot{\gamma}^\alpha = \begin{cases} \dot{\gamma}_0^\alpha \exp\left[-\frac{Q_{slip}}{k_B\theta}\left(1 - \frac{|\tau^\alpha| - \tau_{pass}^\alpha}{\tau_{cut}^\alpha}\right)\right]\text{sign}(\tau^\alpha) & |\tau^\alpha| > \tau_{pass}^\alpha \\ 0 & |\tau^\alpha| \leqslant \tau_{pass}^\alpha \end{cases} \tag{11}$$

here Q_{slip} is the activation energy for dislocation slip, the pre-exponential variable $\dot{\gamma}_0^\alpha$ is the upper limit of the shear rate for the case that the Boltzmann factor is equal to one in Eq. (11)

$$\dot{\gamma}_0^\alpha = \frac{k_B\theta v_0}{c_1 c_3 G b^2}\sqrt{\rho_P^\alpha} \tag{12}$$

---

[1] In this model the maximization process is applied to each individual slip system seperately. One could argue that a global optimization should be used, however, we assume, that there will not be a big difference due to two reasons: firstly there are only very few slip systems active locally (sometimes even just one in the bulk, however more near boundaries), secondly even though there is some coupling between the individual slip systems this is not very strong and the behaviour of a single slip systems is mostly determined by the resolved shear stress.

[2] The flow rule actually is derived by inserting Eq. (9) into the Orowan equation.

where v_0 is the attack frequency; $\tau_{\mathrm{pass}}^{\alpha}$ is the passing stress, caused by the parallel dislocations

$$\tau_{\mathrm{pass}}^{\alpha} = c_1 G b \sqrt{\rho_{\mathrm{P}}^{\alpha}} \tag{13}$$

and $\tau_{\mathrm{cut}}^{\alpha}$ the cutting stress at 0 K caused by the forest dislocations

$$\tau_{\mathrm{cut}}^{\alpha} = \frac{Q_{\mathrm{slip}}}{c_2 c_3 b^2} \sqrt{\rho_{\mathrm{F}}^{\alpha}} \tag{14}$$

3. Evolution of the densities of the statistically stored and geometrically necessary dislocations

3.1. The evolution of the statistically stored dislocation density

There are four processes contributing to the evolution of the immobile SSDs. The lock forming mechanism between mobile dislocations and forest dislocations $(\dot{\rho}_{\mathrm{SSD}}^{\alpha+})_{\mathrm{locks}}$, and the dipole forming mechanism between mobile dislocations with anti-parallel Burgers vector $(\dot{\rho}_{\mathrm{SSD}}^{\alpha+})_{\mathrm{dipole}}$ determine the multiplication terms, while the athermal annihilation of two parallel dislocations with anti-parallel Burgers vector within a critical distance $(\dot{\rho}_{\mathrm{SSD}}^{\alpha-})_{\mathrm{athermal}}$ and the thermal annihilation by climb of edge dislocations $(\dot{\rho}_{\mathrm{SSD}}^{\alpha-})_{\mathrm{thermal}}$ determine the annihilation terms. The complete rate equation for the immobile SSD combines these four processes, see Ma and Roters (2004) for a detailed derivation

$$\dot{\rho}_{\mathrm{SSD}}^{\alpha} = (\dot{\rho}_{\mathrm{SSD}}^{\alpha+})_{\mathrm{locks}} + (\dot{\rho}_{\mathrm{SSD}}^{\alpha+})_{\mathrm{dipole}} + (\dot{\rho}_{\mathrm{SSD}}^{\alpha-})_{\mathrm{athermal}} + (\dot{\rho}_{\mathrm{SSD}}^{\alpha-})_{\mathrm{thermal}} \tag{15}$$

$$(\dot{\rho}_{\mathrm{SSD}}^{\alpha+})_{\mathrm{locks}} = c_4 \sqrt{\rho_{\mathrm{F}}^{\alpha}} \dot{\gamma}^{\alpha} \tag{16}$$

$$(\dot{\rho}_{\mathrm{SSD}}^{\alpha+})_{\mathrm{dipole}} = c_6 d_{\mathrm{dipole}}^{\alpha} \rho_{\mathrm{M}}^{\alpha} \dot{\gamma}^{\alpha} \tag{17}$$

$$(\dot{\rho}_{\mathrm{SSD}}^{\alpha-})_{\mathrm{athermal}} = -c_5 \rho_{\mathrm{SSD}}^{\alpha} \dot{\gamma}^{\alpha} \tag{18}$$

$$(\dot{\rho}_{\mathrm{SSD}}^{\alpha-})_{\mathrm{thermal}} = -c_7 \exp\left(-\frac{Q_{\mathrm{bulk}}}{k_{\mathrm{B}}\theta}\right) \frac{|\tau^{\alpha}|}{k_{\mathrm{B}}\theta} (\rho_{\mathrm{SSD}}^{\alpha})^2 \dot{\gamma}^{c_s} \tag{19}$$

where c_4–c_8 are constants, d_{dipole} is the critical distance for dipole formation, and Q_{bulk} is the activation energy for self-diffusion.

3.2. The evolution of the geometrically necessary dislocation density

When orientation gradients are present in a volume portion GNDs must be introduced to preserve the continuity of the lattice. A relation between a possible GND measure and the plastic deformation gradient has been proposed by Nye (1953). This approach has been later extended to a more physically motivated continuum approach to generally account for strain gradient effects by Dai and Parks (1997) and Dai (1997). Following this approach we use as a dislocation density tensor for a selected volume portion and Burgers circuit

$$\mathbf{\Lambda} = -\frac{1}{b}\left(\mathbf{\nabla}_X \times \mathbf{F}_{\mathrm{P}}^{\mathrm{T}}\right)^{\mathrm{T}} \tag{20}$$

where nabla, $\mathbf{\nabla}_X$, is defined as the derivative with respect to the reference coordinates, i.e. $\mathbf{\nabla}_X = \partial/\partial\mathbf{X}$. When using the material time derivative of Eq. (20) and the result from Eq. (3) we obtain

$$\dot{\mathbf{\Lambda}} = \sum_{\alpha=1}^{N} \dot{\mathbf{\Lambda}}^{\alpha} \tag{21}$$

It is not straightforward to project $\mathbf{\Lambda}$ into forest and parallel dislocations because the tangent vector of the GNDs is not constant. Although in this paper SSDs are assumed to be edge dislocations only, for the GND analysis we have to account for both, edge and screw dislocations. $\dot{\mathbf{\Lambda}}^{\alpha}$ can then be decomposed into three groups of dislocations, namely, one group of screw dislocations with their tangent vector parallel to the slip direction $\tilde{\mathbf{d}}^{\alpha}$, and two groups of edge dislocations with their respective tangent vectors parallel to $\tilde{\mathbf{n}}^{\alpha}$ and $\tilde{\mathbf{t}}^{\alpha}$, i.e.
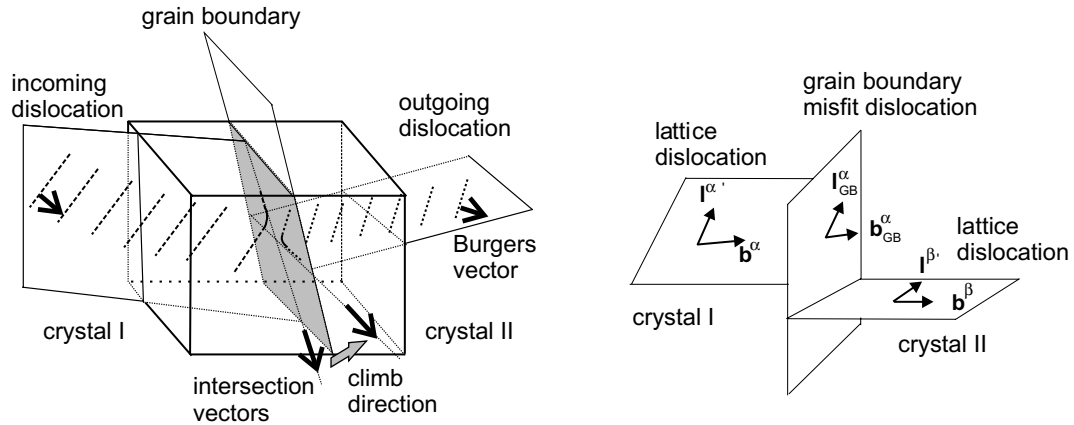
Fig. 2. Schematic drawing of a penetration event from crystal I to crystal II.

$$\dot{\mathbf{\Lambda}}^{\alpha} = \dot{\mathbf{\Lambda}}_{s}^{\alpha} + \dot{\mathbf{\Lambda}}_{en}^{\alpha}4 + \dot{\mathbf{\Lambda}}_{et}^{\alpha} \tag{22}$$

where the three dislocation tensors amount to

$$\dot{\mathbf{\Lambda}}_{s}^{\alpha} = -\dot{\rho}_{GNDs}^{\alpha}\tilde{\mathbf{d}}^{\alpha} \otimes \tilde{\mathbf{d}}^{\alpha} \tag{23}$$

$$\dot{\mathbf{\Lambda}}_{et}^{\alpha} = -\dot{\rho}_{GNDet}^{\alpha}\tilde{\mathbf{d}}^{\alpha} \otimes \tilde{\mathbf{t}}^{\alpha} \tag{24}$$

$$\dot{\mathbf{\Lambda}}_{en}^{\alpha} = -\dot{\rho}_{GNDen}^{\alpha}\tilde{\mathbf{d}}^{\alpha} \otimes \tilde{\mathbf{n}}^{\alpha} \tag{25}$$

and the scalar dislocation densities to

$$\dot{\rho}_{GNDs}^{\alpha} = \frac{1}{b}\left(\mathbf{\nabla}_{X} \times (\dot{\gamma}^{\alpha}\mathbf{F}_{P}^{T}) \cdot \tilde{\mathbf{n}}^{\alpha}\right) \cdot \tilde{\mathbf{d}}^{\alpha} \tag{26}$$

$$\dot{\rho}_{GNDet}^{\alpha} = \frac{1}{b}\left(\mathbf{\nabla}_{X} \times (\dot{\gamma}^{\alpha}\mathbf{F}_{P}^{T}) \cdot \tilde{\mathbf{n}}^{\alpha}\right) \cdot \tilde{\mathbf{t}}^{\alpha} \tag{27}$$

$$\dot{\rho}_{GNDen}^{\alpha} = \frac{1}{b}\left(\mathbf{\nabla}_{X} \times (\dot{\gamma}^{\alpha}\mathbf{F}_{P}^{T}) \cdot \tilde{\mathbf{n}}^{\alpha}\right) \cdot \tilde{\mathbf{n}}^{\alpha} \tag{28}$$

For the details behind the derivation of these equations, we refer to Ma et al. (2006a).

4. A grain boundary micro-mechanical mechanism based on dislocation transmission

In this chapter we discuss the mathematical treatment of the grain boundary resistance against slip in the constitutive description of one material point as introduced in Ma et al. (2006b). We consider two crystals with orientations $\mathbf{Q}_{I}$ and $\mathbf{Q}_{II}$ with slip systems $(\mathbf{d}^{\alpha,\beta}, \mathbf{t}^{\alpha,\beta}, \mathbf{n}^{\alpha,\beta})$, $\alpha, \beta = 1, 2, \ldots, 12$,[3] and a grain boundary with a normal vector $\mathbf{n}_{GB}$, which separates these two crystals, see Fig. 2.

We assume, that the dislocation line elements, $\mathbf{l}^{\alpha'}$ and $\mathbf{l}^{\beta'}$, will align with the boundary plane during the transmission event. This means that in the moment of the boundary penetration instead of $\mathbf{l}^{\alpha'}$ and $\mathbf{l}^{\beta'}$ we encounter the two line elements

$$\mathbf{l}^{\alpha} = l^{\alpha'}(\mathbf{n}_{GB} \times \mathbf{n}^{\alpha}) \tag{29}$$

$$\mathbf{l}^{\beta} = l^{\beta'}(\mathbf{n}_{GB} \times \mathbf{n}^{\beta}) \tag{30}$$

In order to conserve the lattice defect as expressed by the dislocation tensor during the penetration step the following equation must be satisfied:

---

[3] The indices α and β always refer to crystals I and II, respectively. In case of a penetration from crystal II into crystal I α and β have to be exchanged.

$$\mathbf{b}^\alpha \otimes \mathbf{l}^\alpha = \mathbf{b}^\beta \otimes \mathbf{l}^\beta + \mathbf{b}^\alpha_{GB} \otimes \mathbf{l}^\alpha_{GB} \tag{31}$$

where $\mathbf{b}$ is the respective Burgers vector and the index GB refers to the grain boundary dislocation, i.e. to the debris which remains in or at the grain boundary upon slip penetration.

The energy of formation for these misfit dislocations upon a slip penetration event fulfills the following inequality:

$$\frac{1}{2} G b^{\alpha^2} l^\alpha \leqslant \frac{1}{2} G b^{\beta^2} l^\beta + \frac{1}{2} G b^\alpha_{GB}{}^2 l^\alpha_{GB} \tag{32}$$

where G is the shear modulus. As both mobile dislocations in grains I and II are crystal dislocations, we assume that they have equal energies. Therefore, the additional barrier energy for the transmission event is the energy of formation of the grain boundary dislocation additionally formed during the process.[4] The final task is to identify for every slip system α of crystal I a slip system β in crystal II with the boundary condition that the energy of the grain boundary dislocation is minimized upon slip transmission

$$E^\alpha_{GB} = \min_\beta \frac{1}{2} G b^\alpha_{GB}{}^2 l^\alpha_{GB} \tag{33}$$

As shown in Ma et al. (2006b) this expression does not have a unique solution. Nevertheless when we assume that the Burgers vector of the grain boundary dislocation has the same magnitude as the lattice dislocations, and for a mobile dislocation with the length b,[5] Eq. (33) can be simplified as

$$E^\alpha_{GB} = a^\alpha \left(\frac{1}{2} G b^3 \right) \tag{34}$$

$$a^\alpha = \min_\beta (\| \mathbf{d}^\alpha \otimes \mathbf{t}^\alpha - \mathbf{d}^\beta \otimes \mathbf{t}\beta \|) \tag{35}$$

where $\mathbf{d}^{\alpha,\beta}$ and $\mathbf{t}^{\alpha,\beta}$ are unit vectors along $\mathbf{b}^{\alpha,\beta}$ and $\mathbf{l}^{\alpha,\beta}$, respectively.

Finally one has to consider two special situations: first, when the grain boundary plane is parallel to the slip plane of the incoming dislocation the energy barrier is set to zero, because the mobile dislocations do not penetrate the grain boundary, but they move parallel to it; second, when the plane of the outgoing dislocation is parallel to the grain boundary we set $\mathbf{l}^\beta$ parallel to $\mathbf{l}^\alpha$ as there is no intersection line with the grain boundary.

In summary the new model developed in this paragraph provides an obstacle strength of the grain boundary which does not only depend on the grain boundary misorientation but also on the grain boundary plane orientation ($\mathbf{n}_{GB}$) and on the slip systems involved on either side of the interface.

5. The grain boundary element

In general, in CP-FEM implementations the grain boundaries coincide with element boundaries. In contrast to this approach we introduced a special grain boundary element in Ma et al. (2006b), where one half of the Gauss points belong to one crystal, while the others reside in the second crystal, see Fig. 3. The constitutive law of the material points belonging to this element, comprises a set of equations including the cutting and penetration mechanisms (Ma et al., 2006b), namely

$$\dot{\gamma}^\alpha = \begin{cases} \dot{\gamma}^\alpha_0 \exp\left[-\frac{Q_{eff}}{k_B \theta} \left(1 - \frac{|\tau^\alpha| - \tau^\alpha_{pass}}{\tau^\alpha_{cut}} \right) \right] \text{sign}(\tau^\alpha) & |\tau^\alpha| > \tau^\alpha_{pass} \\ 0 & |\tau^\alpha| \leqslant \tau^\alpha_{pass} \end{cases} \tag{36}$$

---

[4] A remark on the misfit dislocations: While they serve as a means to quantify the penalty energy they will very likely not be stored but be dissolved by some relaxation process in the grain boundary. This implies that there will be no accumulation of misfit dislocations in the boundary, which would alter the process for newly incoming dislocations. Moreover, the assumption that the general character of the grain boundary is not altered by the penetration process allows us to use the same model of the penetration process for small strains and large strains.

[5] Choosing b gives at least a reasonable order of magnitude. Any other choice would just alter the value of the constant a. Finally there would be no difference in the modelling, as the fitting parameter c_9 is introduced, which would eventually take a different value.
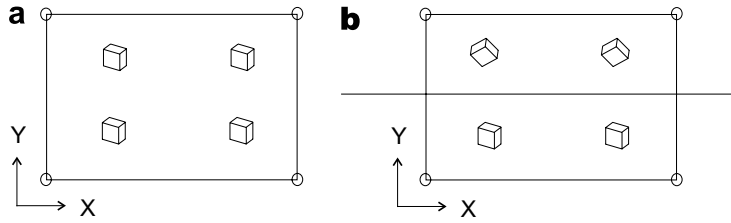
Fig. 3. 2D schematic drawing of a bulk element (a) and a grain boundary element (b) in their initial state. During the deformation GNDs should preserve the continuity of lattice in *X*- and *Y*-direction for bulk elements, while for grain boundary elements only the *X*-direction is considered.

where the pre-exponential variable $\dot{\gamma}_0^\alpha$ and the passing stress $\tau_{\text{pass}}^\alpha$ are the same as in Eqs. (12) and (13), the cutting stress caused jointly by the forest dislocations and the grain boundary at 0 K reads

$$\tau_{\text{cut}}^\alpha = \frac{Q_{\text{eff}}}{c_2 c_3 b^2} \sqrt{\rho_F^\alpha} \tag{37}$$

and an effective activation energy is used instead of Q_{slip}

$$Q_{\text{eff}} = Q_{\text{slip}} + Q_{\text{GB}}^\alpha \tag{38}$$

$$Q_{\text{GB}}^\alpha = c_9 E_{\text{GB}}^\alpha \tag{39}$$

where c_9 is a fitting parameter.

Modifying the activation energy for an individual dislocation jump in Eq. (36) implies that the boundary is overcome in a single activation event. The activation area for this event is of the order $\lambda^\alpha b$. In this expression λ^α is the trapping length of the mobile dislocation (see Fig. 4(a)) and b is the magnitude of the lattice Burgers vector, which is used as obstacle width for the forest dislocation density. However, when simply adding the activation energies, we use the same activation area for the transmission event. Therefore, the element thickness of the boundary element should amount to a value close to b (see Fig. 4(b)). If we further assume that we start with a mesh of brick elements the element volume ($b\lambda^\alpha\lambda^\alpha$) would be of the order of 1 μm³ or less. Even if we use small samples in the mm size range, this would require the use of about one billion elements for meshing the sample. This number is out of range for practical applications.

The only way to circumvent this problem is to increase the element thickness to L_{GB} (Fig. 4(c)). However, by doing so we assign an overly stiff material behavior to a volume much bigger than the actual grain boundary volume. In order to compensate for this large volume we can artificially decrease the grain boundary strength by the choice of the constant $c_9 \propto \frac{b}{L_{\text{GB}}}$. It has to be stressed though, that this is a purely empirical adjustment due to the use of larger finite elements and does not describe the scaling of the underlying physics one-to-one. Therefore in this paper we study the influence of the choice of c on the *local* distribution of stress and strain on the example of a simple shear test.

6. Simple shear tests

6.1. Experimental and FEM setup

The experimental set-up and the region studied are shown in Fig. 5. In order to study the grain boundary behavior a rather fine mesh is generated which contains $240 \times 41 \times 1$ 3D brick elements. The initial element shape is cubic with an edge length of 10 μm, which implies $L_{\text{GB}} = 10$ μm The grain boundary elements are placed in the the *XZ*-plane in the middle of the *Y* extension of the mesh. In these newly introduced grain boundary elements each set of four integration points on either side of the interface carries the initial orientations of the abutting crystals as shown in Fig. 3. In these elements, which initially contain a change in crystal orientation within their element borders according to the real bicrystal, the new constitutive grain boundary
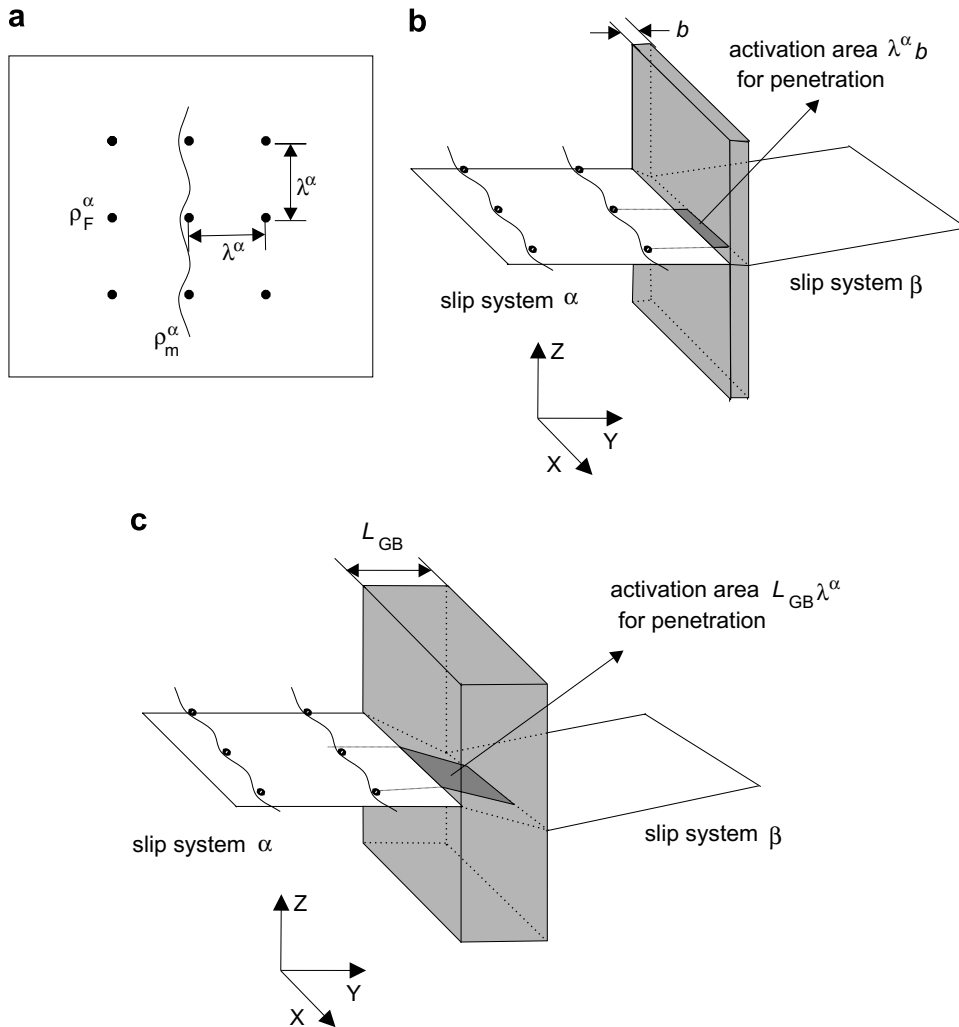
Fig. 4. Schematic drawing of the penetration and cutting mechanism: (a) cutting mechanism; (b) penetration of perfect grain boundary; (c) FEM treatment of penetration process.

law applies, resulting in a locally increased stiffness in terms of an additional energy barrier for each incoming slip system as outlined above. Even though there is only one element layer the simulation is fully 3D, i.e. deformation is not restricted to plane strain.

The orientation data obtained from the micro-texture measurements is expressed as $(\varphi_1, \Phi, \varphi_2)$ in Bunge–Euler notation in the RD-TD-ND coordinate system. For the finite element analysis the global coordinate system was defined by X parallel to RD, Y parallel to TD and Z parallel to ND. This means that the measured initial orientations were directly assigned to the respective integration points.

To study the influence of the grain boundary element five different simulations were performed for two bicrystals:

(1) no strain gradient and no grain boundary penalty (i.e. local, $c_9 = 0$);
(2) no strain gradient and high grain boundary penalty (i.e. local, $c_9 = 5$);
(3) with strain gradient and no grain boundary penalty (i.e. nonlocal, $c_9 = 0$);
(4) with strain gradient and normal grain boundary penalty (i.e. nonlocal, $c_9 = 1$);
(5) with strain gradient and high grain boundary penalty (i.e. nonlocal, $c_9 = 5$).
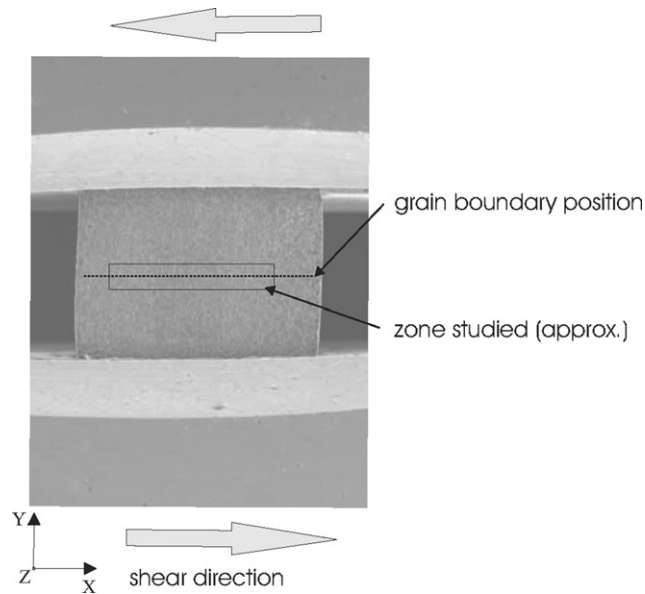
Fig. 5. Experimental set-up and the position of the studied zone across the grain boundary.

Here $c_9 = 0$ means no grain boundary penalty, while high values of c_9 coincide with the case of a non-shearable grain boundary.

The first bicrystal had a 7.4° small angle grain boundary with the initial orientations ($\varphi_1 = 277.0°$, $\Phi = 32.3°$, $\varphi_2 = 37.4°$)$_I$ and ($\varphi_1 = 264.7°$, $\Phi = 32.3°$, $\varphi_2 = 44.3°$)$_{II}$ and the second bicrystal had a 33° grain boundary with the initial orientations ($\varphi_1 = 105.9°$, $\Phi = 34.1°$, $\varphi_2 = 43.4°$)$_I$ and ($\varphi_1 = 64.1°$, $\Phi = 34.8°$, $\varphi_2 = 54.6°$)$_{II}$ (Zaefferer et al., 2003; Kuo, 2004). All simulations are performed using the same model parameters as in Ma et al. (2006a,b) with the exception of parameter c_9 (see Table 1).

6.2. Misorientation in the grain boundary region

Fig. 6 shows the grain boundary area of the two bicrystals after deformation. It can be seen, that the deformation in both cases is not homogeneous but some deformation patterning is visible especially in the lower crystals (Crystal I). These structures most likely result from dislocation cell and slip band formation, which cannot be treated within the framework of the presented model.

To average out the effect of these deformation patterns on the measured misorientation toward the original orientation of the crystals it was measured along 10 paths on either side of the boundary, where it was tried to

Table 1
The parameters of the nonlocal dislocation model for pure aluminum crystals

Symbol	Value	Meaning
Q_{slip}	3.0×10^{-19} J	Activation energy for slip
Q_{bulk}	2.4×10^{-19} J	Activation energy for climb
c_1	0.1	Constant for passing stress
c_2	2.0	Constant for jump width
c_3	1.0	Constant for obstacle width
c_4	1.5×10^7 m^{-1}	Constant for lock forming rate
c_5	10.0	Constant for athermal annihilation rate
c_6	1×10^{-30} m^{-1}	Constant for thermal annihilation rate
c_7	1×10^7 m^5 s^{c_8}	Constant for dipole forming rate
c_8	0.3	Constant for nonlinear climb of edge dislocations
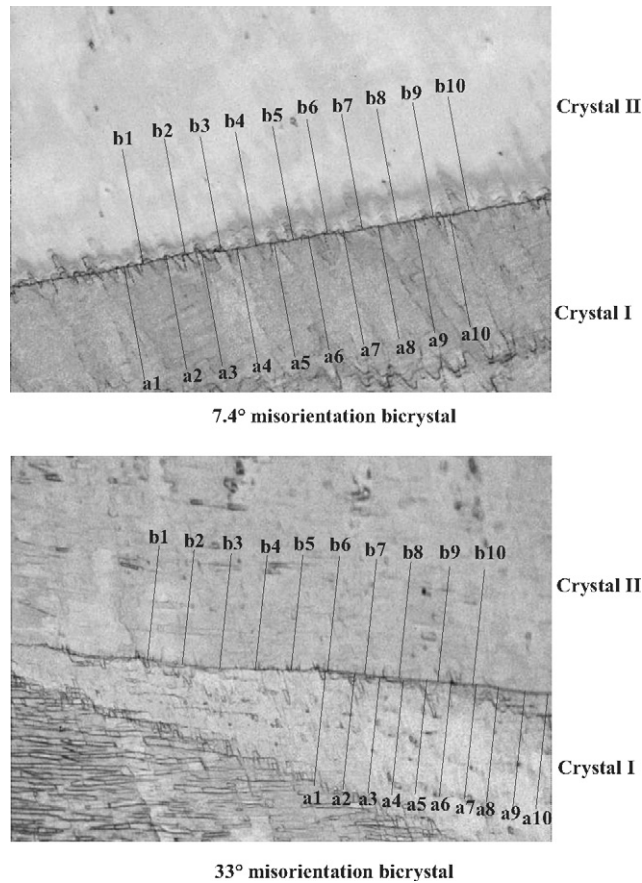
Fig. 6. Positions for misorientation determination in the grain boundary region.

measure in rather homogeneous areas as shown in Fig. 6. The average misorientation calculated from these 10 paths is plotted in Fig. 7 for both bicrystals. The high misorientation values for the small angle bicrystal probably result from a rigid body rotation when remounting the sample after the deformation experiment. Therefore we will concentrate on the difference in misorientation between the two crystals in what follows.

For the 7.4° bicrystal, the misorientation gradient extents to both abutting crystals. Here it is important to point out that a maximum respective minimum appears just away from the grain boundary in both crystals,
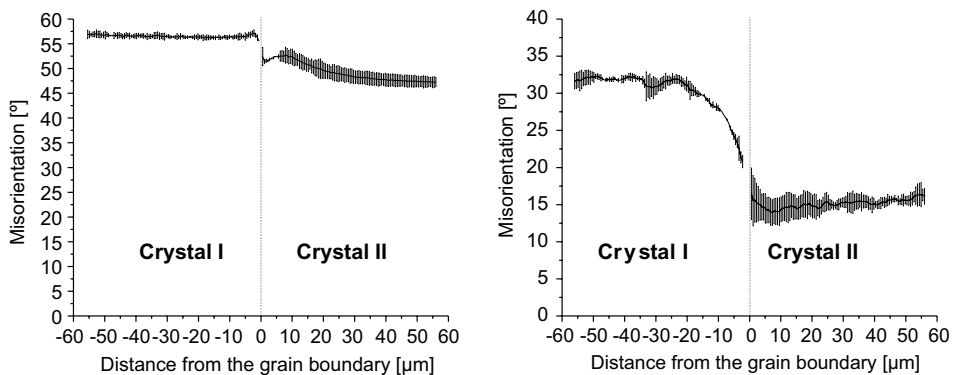
Fig. 7. Average misorientation relative to the initial orientation measured for the two bicrystals.

see Fig. 7. This can be attributed to the local microstructure caused by a slip band near the boundary. The difference in misorientation between crystals I and II varies between 5° and 10°.

In the 33° bicrystal, the path lines do not cross microstructural features. As a result the misorientation changes rather smoothly from one abutting crystal to the other. In comparison with the small angle bicrystal, it is remarkable that in the large angle crystal the misorientation shows a strong gradient in crystal I. The maximum difference in misorientation amounts to about 18°.

The ultimate goal of any micro-structural model has to be the correct prediction of the *local* mechanics and micro-structures. In Fig. 8 we, therefore, compare the local misorientation with respect to the initial orientation along one exemplary line crossing the simulation area from top to bottom. In both cases the difference in
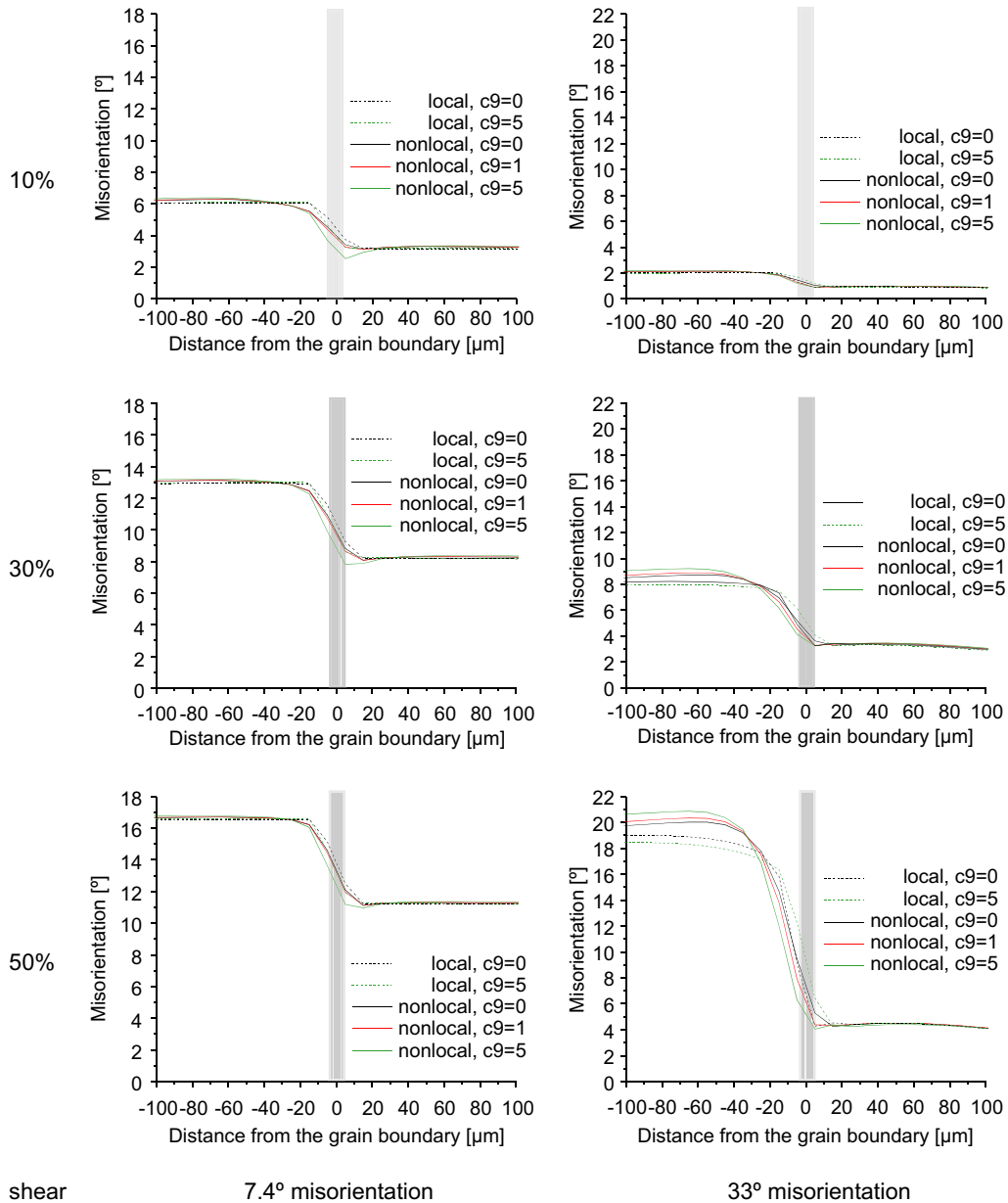
Fig. 8. Misorientation calculated for the two bicrystals for simulation cases (1)–(5). The range of the grain boundary element is indicated by the grey bar.

misorientation after 50% shear shows good agreement with the experiment. However, there are distinct differences between the two bicrystals especially when considering the evolution of the misorientation profile. First of all the misorientation profile is almost independent of the model used for the small angle grain boundary, while for the large angle grain boundary nonlocality and higher grain boundary penalty increase the difference in misorientation between the two crystals. Here the combination of strain gradients and high grain boundary penalty shows the best agreement with the experiment. Second the difference in misorientation saturates rather fast for the small angle grain boundary, it is only shifted toward higher misorientations after 30% shear, while it steadily increases for the large angle grain boundary.

6.3. von Mises equivalent strain in the grain boundary region

The experimental data clearly reveal the strong micro-mechanical effect imposed by the presence of the respective grain boundaries in both bicrystals. Even for the small angle grain boundary (7.4°) the shear
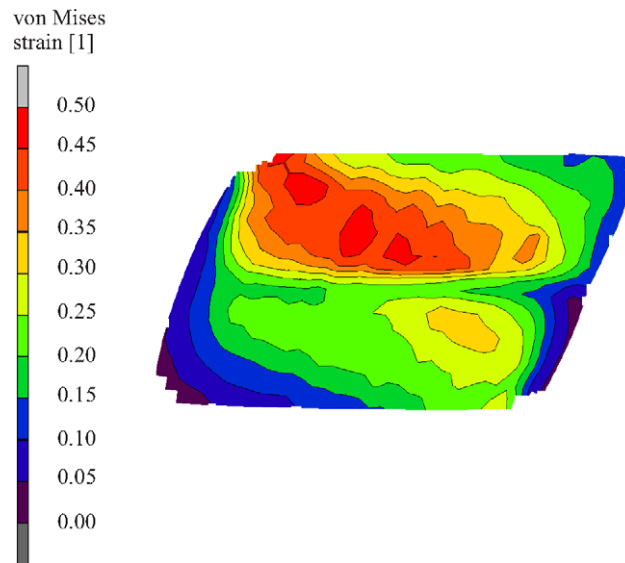
Fig. 9. von Mises strain distribution for the small angle boundary bicrystal after 40% shear.
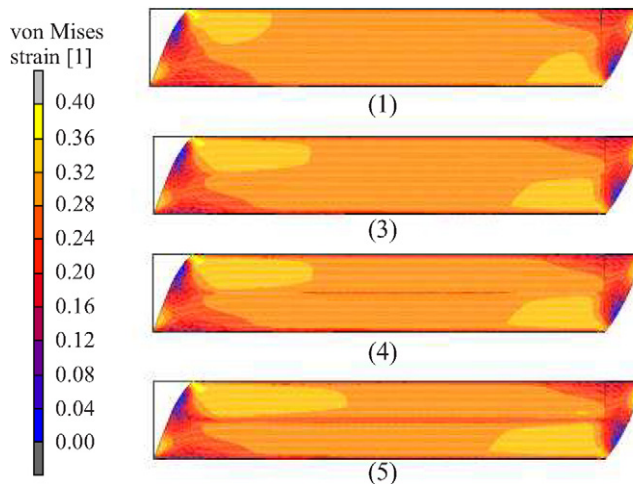
Fig. 10. von Mises strain distribution for simulation cases (1)–(5).

experiment shows a rather inhomogenous distribution of the von Mises strain among the two abutting crystals (Fig. 9). With increasing grain boundary misorientation the heterogeneous distribution of the von Mises strain becomes even more pronounced (Ma et al., 2006b).

For the bicrystal with the large angle grain boundary, the empirical (local) model is capable to predict some although not all characteristics of the strain separation between the two crystals. This partial success in case of the large angle grain boundary, is attributed to the strong effect of the change in the Schmid factor across the interface. In this case the kinematical effect which arises from distinct differences in the slip system selection on either side of a grain boundary plays an essential role.

However, in the case of the small angle boundary it was clearly shown in Ma et al. (2006b), that the combination of strain gradients and a grain boundary penalty results in the best reproduction of the
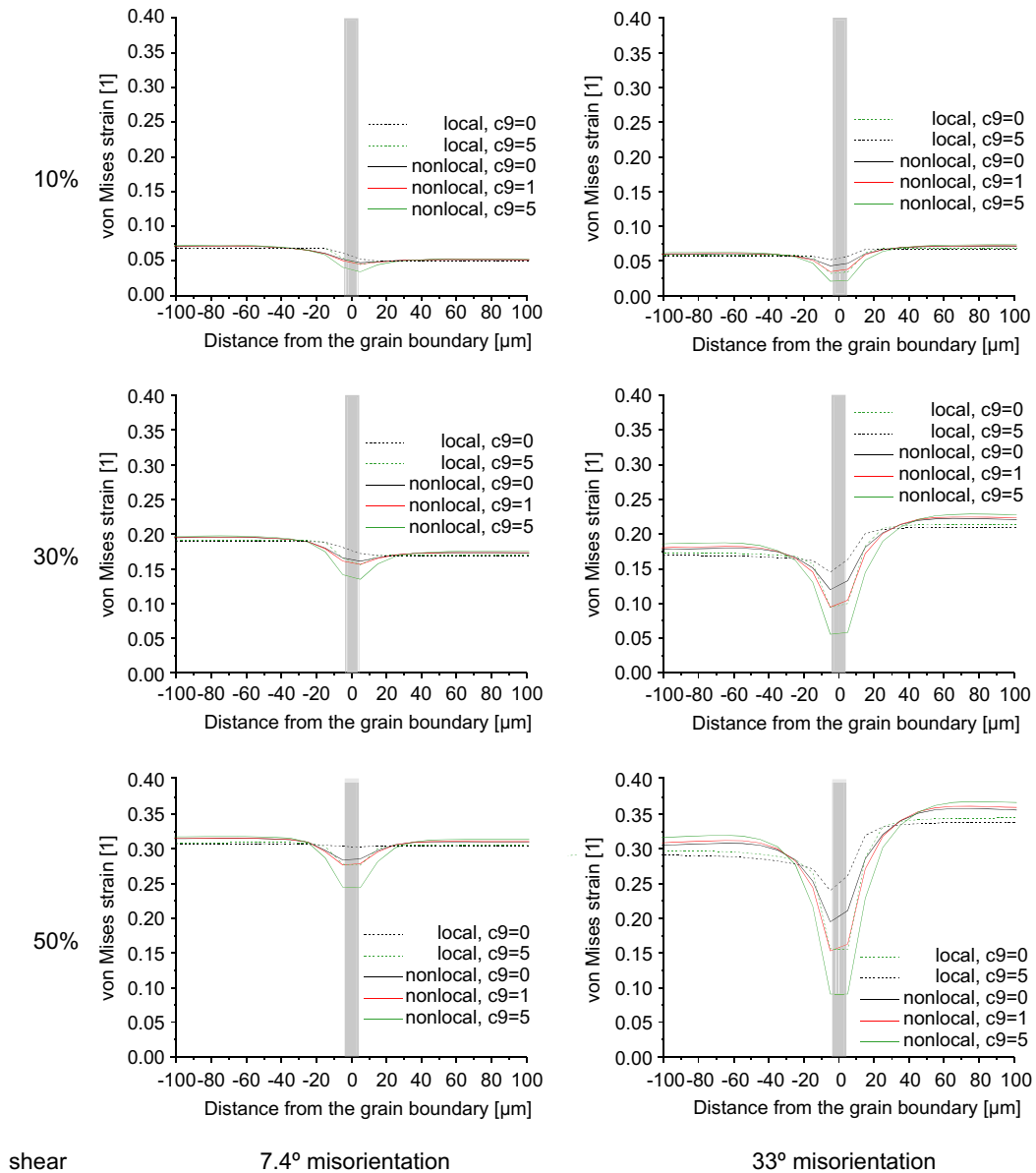
Fig. 11. von Mises strain calculated for the two bicrystals for simulation cases (1)–(5). The range of the grain boundary element is indicated by the grey bar.
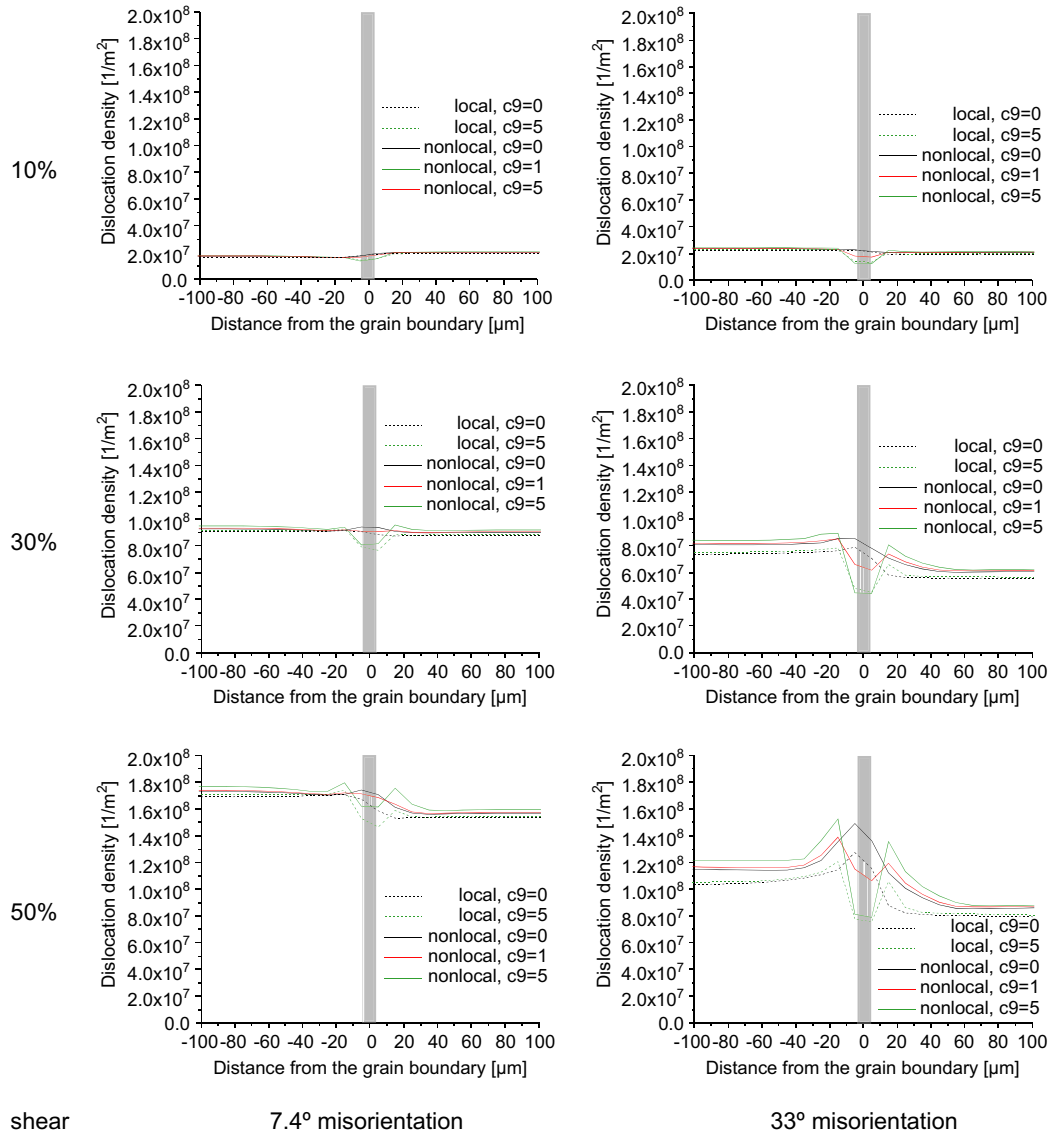
Fig. 12. Statistically stored dislocation density calculated for the two bicrystals for simulation cases (1)–(5). The range of the grain boundary element is indicated by the grey bar.

experimental findings. This is illustrated by Fig. 10, where only for case (5) the grain boundary becomes clearly visible.

Fig. 11 shows the evolution of von Mises strain for the different simulations. The hardening effect (and thus lower deformation) introduced by both the strain gradients and the grain boundary penalty is clearly visible. However as shown above only the combination of both gives a sufficiently strong effect to reproduce the experimental findings.

6.4. Dislocation densities in the grain boundary region

Figs. 12 and 13 show the distribution of the statistically stored dislocations and the geometrically necessary dislocations, respectively, for the different simulation cases. It can be seen, that for the calculations without the grain boundary penalty the SSDs show a maximum at the grain boundary, whereas for the calculations
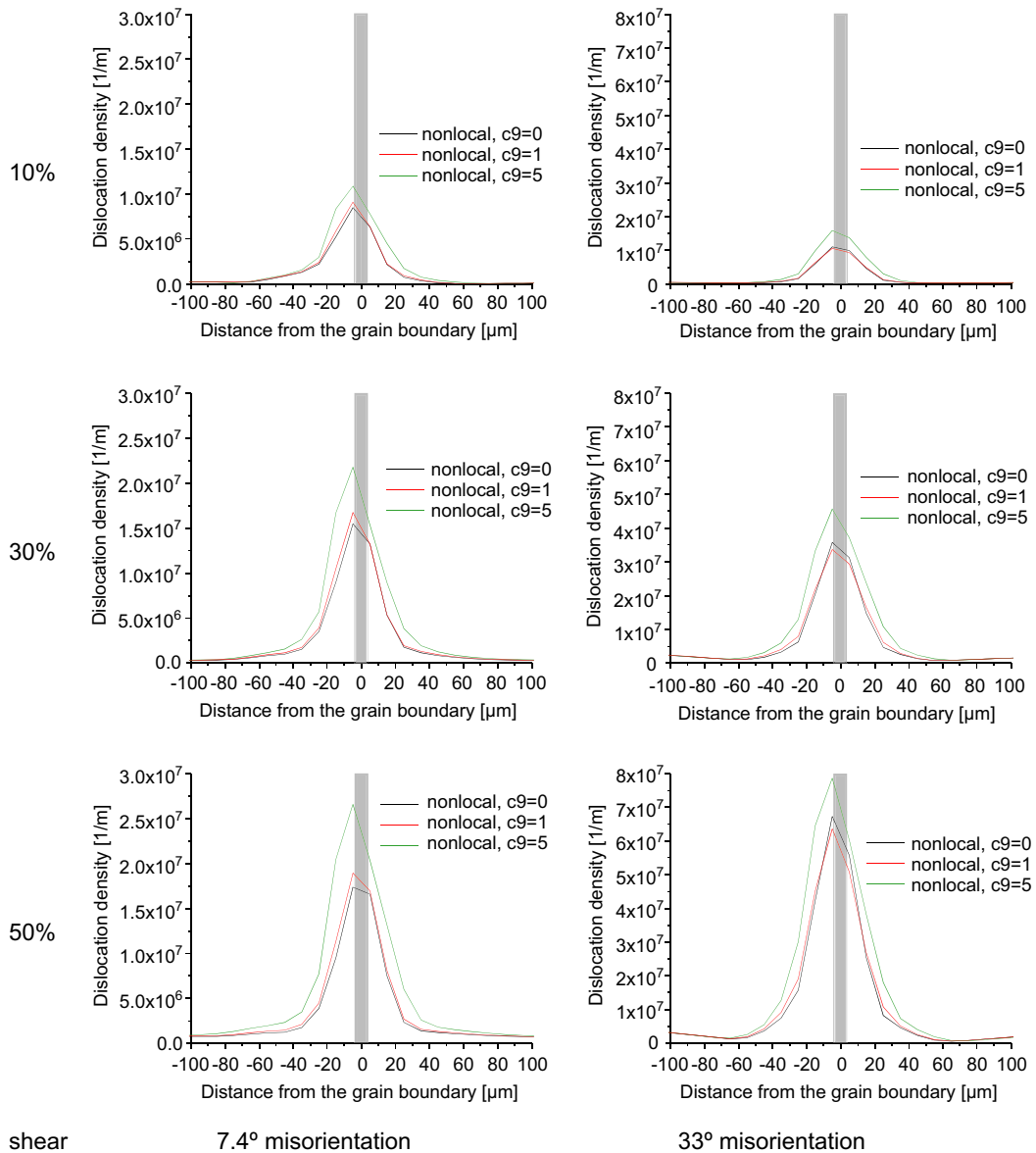
Fig. 13. Geometrically necessary dislocation density calculated for the two bicrystals for simulation cases (1)–(5). The range of the grain boundary element is indicated by the grey bar.

including the grain boundary they exhibit a maximum some distance away from the grain boundary and a strong minimum at the grain boundary. In contrast the geometrically necessary dislocations show a strong maximum at the grain boundary. All distributions become more pronounced with increasing values of parameter c_9, which, therefore, can be used to fine tune the grain boundary effect. While the dislocation densities themselves can hardly be used for this purpose as they cannot be measured with the required accuracy, the width of the distribution of GNDs can serve as a measure, as it coincides with strain gradients that can be measured with high precision.[6] In the examples shown this width is of the order of 100 μm which is about ten times the element size.

---

[6] Unfortunately the resolution of the measurement shown in Fig. 9 is not sufficient for this purpose.

7. Conclusions

The interaction of the mobile dislocations with grain boundaries is introduced via an additional activation energy barrier into the rate equation for the slip of mobile dislocations in the vicinity of grain boundaries. The energy barrier is derived by using a geometrical model for thermally activated dislocation penetration events through grain boundaries. The model takes full account of the geometry of the grain boundaries and of the Schmid factors of the critically stressed incoming and outgoing slip systems.

Several simulations of the simple shear deformation of Al bicrystals have been carried out using a local as well as a nonlocal version of the model with and without grain boundary penalties of different strength. It was clearly shown that only a combination of strain gradient and grain boundary effect is sufficient to reproduce the experimental findings. As compared with other models, that do not allow any slip across the grain boundary (Evers et al., 2004) the model presented here has the advantage that the grain boundary character is taken into account and the new parameter c_9 can be used to fine tune the effect of the grain boundary.

References

Arsenlis, A., Parks, D.M., 2002. Modeling the evolution of crystallographic dislocation density in crystal-plasticity. Journal of the Mechanics and Physics of Solids 50 (9), 1979–2009.

Ashby, M.F., 1970. The deformation of plastically nonhomogenous materials. Philosophical Magazine 21, 399.

Bronkhorst, C.A., Kalidindi, S.R., Anand, L., 1992. Poly crystalline plasticity and the evolution of crystallographic texture in fcc metals. Philosophical Transactions of the Royal Society, Series A (Physical Sciences and Engineering) 341 (1662), 443–477.

Dai, H., 1997. Geometrically-necessary dislocation density in continuum plasticity theory, FEM implementation and applications. Ph.D. thesis, Massachusetts Institute of Technology.

Dai, H., Parks, D.M., 1997. Geometrically-necessary dislocation density and scale-dependent crystal-plasticity. In: Khan, A. (Ed.), Proceedings of Sixth International Symposium on Plasticity. Gordon and Breach, pp. 17–18.

Evers, L.P., Parks, D.M., Brekelmans, W.A.M., Geers, M.G.D., 2002. Crystal-plasticity model with enhanced hardening by geometrically necessary dislocation accumulation. Journal of the Mechanics and Physics of Solids 50 (11), 2403–2424.

Evers, L.P., Brekelmans, W.A.M., Geers, M.G.D., 2004. Scale dependent crystal-plasticity framework with dislocation density and grain boundary effects. International Journal of Solids and Structures 41 (18–19), 5209–5230.

Kalidindi, S.R., Bronkhorst, C.A., Anand, L., 1992. Crystallographic texture evolution in bulk deformation processing of fcc metals. Journal of the Mechanics and Physics of Solids 40, 537–569.

Kuo, J.-C., 2004. Mikrostrukturmechanik von Bikristallen mit Kippkorngrenzen. Ph.D. thesis, RWTH Aachen.

Lee, E.H., 1969. Elastic–plastic deformation at finite strains. Transactions of the ASME Series E, Journal of Applied Mechanics 36 (1), 1–6.

Ma, A., Roters, F., 2004. A constitutive model for fcc single crystals based on dislocation densities and its application to uniaxial compression of aluminium single crystals. Acta Materialia 52 (12), 3603–3612.

Ma, A., Roters, F., Raabe, D., 2004. Numerical study of textures and Lankford values for fcc polycrystals by use of a modified Taylor model. Computational Materials Science 29 (3), 353–361.

Ma, A., Roters, F., Raabe, D., 2006a. A dislocation density based constitutive model for crystal-plasticity FEM including geometrically necessary dislocations. Acta Materialia 54, 2169–2179.

Ma, A., Roters, F., Raabe, D., 2006b. On the consideration of interactions between dislocations and grain boundaries in crystal-plasticity finite element modeling – theory, experiments, and simulations. Acta Materialia 54, 2181–2194.

Nye, J.F., 1953. Some geometrical relations in dislocated crystals. Acta Metallurgica 1, 153–162.

Roters, F., 2003. A new concept for the calculation of the mobile dislocation density in constitutive models of strain hardening. Physica Status Solidi B 240 (1), 68–74.

Taylor, G.I., 1938. Plastic strain in metals. Journal of Institute Metals 62, 307–324.

Van Houtte, P., Li, S., Seefeldt, M., Delannay, L., 2005. Deformation texture prediction: from the Taylor model to the advanced Lamel model. International Journal of Plasticity 21 (3), 589–624.

Zaefferer, S., Kuo, J.-C., Zhao, Z., Winning, M., Raabe, D., 2003. On the influence of the grain boundary misorientation on the plastic deformation of aluminum bicrystals. Acta Materialia 51 (16), 4719–4735.